Title

Role of Catalyst Preparation on the Electrocatalytic Activity of Ni1–x Fe x OOH for the Oxygen Evolution Reaction

Journal

The Journal of Physical Chemistry C, 119(32)

ISSN

1932-7447

Authors

Klaus, Shannon
Louie, Mary W
Trotochaud, Lena
et al.

Publication Date

2015-08-13

DOI

10.1021/acs.jpcc.5b04776

Peer reviewed

THE JOURNAL OF PHYSICAL CHEMISTRY C

Article

pubs.acs.org/JPCC

Role of Catalyst Preparation on the Electrocatalytic Activity of $Ni_{1-x}Fe_xOOH$ for the Oxygen Evolution Reaction

Shannon Klaus,[†] Mary W. Louie,[†] Lena Trotochaud, and Alexis T. Bell*

Joint Center for Artificial Photosynthesis, Materials Science Division, Lawrence Berkeley National Laboratory, Berkeley, California 94720, United States

Department of Chemical and Biomolecular Engineering, University of California, Berkeley, California 94720, United States

Supporting Information

ABSTRACT: $Ni_{1-x}Fe_xOOH$ thin films prepared via cathodic electrodeposition have been demonstrated to be highly active catalysts for the oxygen evolution reaction (OER) in basic media. Integration of these catalysts with light-absorbing semiconductors is required for photoelectrochemical fuel generation. However, the application of cathodic potentials required for typical electrochemical catalyst deposition limits the library of compatible photoanode materials. Sputter deposition of catalysts circumvents this limitation by enabling facile catalyst layering without cathodic potentials. In this work, we compare the structure and OER activity of sputter-deposited and electrodeposited $Ni_{1-x}Fe_xOOH$ thin films. Electrochemical cycling converts sputtered $Ni_{1-x}Fe_x$ metallic films to the desired oxides/(oxy)hydroxides. Both film preparation methods give catalysts with similar electrochemical behavior across all compositions. Additionally, OER activity is comparable between the deposition methods, with maximum activity for films with ~20% Fe content (320 mV overpotential at j = 10 mA cm^{-2} geometric). Electrochemical cycling to convert sputtered metallic $Ni_{1-x}Fe_x$ films to metal oxides/(oxy)hydroxides is found to lower the Fe/Ni ratio, while the electrodeposited films exhibit comparable Fe/Ni ratios before and after electrochemical cycling and characterization. Structurally, Fe is found to incorporate within the $Ni(OH)_2$/NiOOH lattice for films formed through both sputter-deposition and electrodeposition. Layered films were also compared to codeposited 1:1 Fe/Ni films. It is found that, for layered films, an Fe top layer inhibits the electrochemical conversion of metallic Ni to $Ni(OH)_2$/NiOOH, thus reducing the amount of $Ni_{1-x}Fe_xOOH$ OER-active phase formed. In contrast, migration of metals within Ni-on-top films occurs readily during electrochemical cycling, resulting in films that are structurally and electrochemically indistinguishable from codeposited $Ni_{1-x}Fe_xOOH$. These findings enable direct application of $Ni_{1-x}Fe_xOOH$ sputtered films to a wider library of photoanodes for light-driven water-splitting applications.

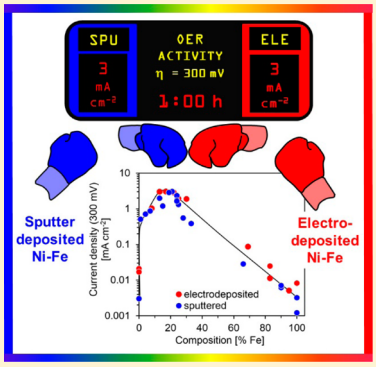

1. INTRODUCTION

Nickel−iron (oxy)hydroxides ($Ni_{1-x}Fe_xOOH$) have been demonstrated as some of the best electrocatalysts for the oxygen evolution reaction (OER) in alkaline electrolytes,[1−5] with catalytic activities that surpass those of precious-metal iridium oxide catalysts.[2] $Ni_{1-x}Fe_xOOH$ and other OER catalysts have recently received renewed interest for application in photoelectrochemical devices for solar energy conversion and storage.[6−12] One of the most commonly reported preparation methods for $Ni_{1-x}Fe_xOOH$ is cathodic electrodeposition from a solution of nickel and iron sulfate and/or nitrate salts,[13−17] but such deposition conditions may not be amenable to integration with many semiconductor photoanode materials. The composition and uniformity of electrodeposited catalyst films can be greatly influenced by the lower electrical conductivity of semiconductors relative to the metallic substrates often used for study of the intrinsic catalyst properties.[8,9,18] Furthermore, the surfaces of oxide photoanodes, such as hematite or bismuth vanadate, can be reduced under the cathodic deposition conditions, greatly affecting the properties of the photoanode and photoanode−catalyst interface.[8,19]

High-efficiency photoelectrochemical devices can only be realized by enabling successful integration of electrocatalyst and photoanode materials in a way that minimally alters the optimized properties of the individual components. Physical vapor deposition methods may therefore be preferable to electrodeposition for coupling of electrocatalysts with certain photoanode substrates. Sputter deposition provides greater flexibility when choosing a substrate material (as electrochemical stability and electrical conductivity of the substrate are not important deposition parameters), ease of catalyst composition control, and high catalyst uniformity across the substrate. Considering the complexity and number of the different processes that occur at photoelectrode-catalyst interfaces,[8,19−21] it is essential to understand whether changing the method of catalyst preparation alone influences catalyst activity and stability. To our knowledge, there is only one previous study of $Ni_{1-x}Fe_xOOH$ OER catalysts prepared by

Received: May 19, 2015
Revised: July 18, 2015
Published: July 19, 2015

DOI: 10.1021/acs.jpcc.5b04776
J. Phys. Chem. C 2015, 119, 18303−18316

sputter deposition.[22] Miller and Rocheleau found that sputtered iron-doped NiO_x produced a more uniform catalyst layer with greater adhesion to the Ni substrate compared to electrodeposited Fe-doped NiO_x, enabling over 7000 h of film stability under OER conditions. However, their work only investigated Fe contents below 6% (percent of total metals − maximum activity was found at 5.2% Fe, the highest codeposited Fe amount in the study). Furthermore, activities of sputtered films were compared to electrodeposited film activities presented in a previous study by Corrigan,[15] and differences could arise due to variations between the two studies in substrate roughness, film active surface area, and other film properties and characterization methods.[15,22]

In this work, we present a detailed study of $Ni_{1-x}Fe_xOOH$ OER electrocatalysts across the entire composition range for both electrodeposited and sputtered films. We demonstrate that $Ni_{1-x}Fe_xOOH$ catalysts prepared by either method have essentially indistinguishable electrochemical behavior and OER activity, and the Fe/Ni ratio yielding optimal OER activity for sputtered films is well within the range of that measured here (and previously) for electrodeposited $Ni_{1-x}Fe_xOOH$. In addition, we show that the extended electrochemical cycling required to fully convert sputtered $Ni_{1-x}Fe_x$ metallic films to the OER active (oxy)hydroxides results in a significant decrease in the film Fe content. Once electrochemical conversion of sputtered $Ni_{1-x}Fe_x$ metal to $Ni_{1-x}Fe_xOOH$ is complete, however, the Fe/Ni ratio remains stable during ∼2 h of oxygen evolution activity measurements. We also investigate differences in catalyst structure and activity due to cosputtering vs layered-sputtering of Ni and Fe. This study provides a direct comparison of these different film preparation methods, demonstrating that highly active OER catalysts can be generated through either sputter deposition or electrodeposition. The availability of sputter-deposited $Ni_{1-x}Fe_xOOH$ with high catalytic activity and stability indistinguishable from electrodeposited $Ni_{1-x}Fe_xOOH$ may be advantageous for integration of these catalysts with certain semiconductor photoanode materials.

2. EXPERIMENTAL SECTION

2.1. Preparation of Catalyst Films. Electrocatalyst films were either electrodeposited or sputter-deposited onto gold rotating disc electrodes (Pine Research Instrumentation). The gold electrodes (5 mm diameter) were fabricated from 99.95% purity (DOE Business Center for Precious Metals Sales and Recovery, BCPMSR). Prior to electrodeposition or sputter deposition, Au discs were polished mechanically with 1 and 0.05 μm alumina slurries, with 10 min of sonication in ultrapure water (18.2 MΩ cm, EMD Millipore) after each polishing step. The Au surface was then stabilized through electrochemical cycling in 0.1 M "Fe-free" KOH from −1.0 to 0.7 V vs Hg/HgO (CH Instruments, filled with 1 M KOH) at 10 mV s^{-1} for ∼30 cycles. Fe-free KOH electrolyte was obtained by following a procedure similar to that of Trotochaud et al.,[23] in which powders of $Ni(OH)_2$ are used to purify KOH solutions. The exact procedure used in this work is provided in the Supporting Information (SI S1). The electrodes were then briefly rinsed with ultrapure water and dried under a N_2 gas stream prior to film deposition.

Films produced by electrodeposition and sputter deposition were targeted to contain ∼3−4 × 10^{15} metal atoms (∼2 nm thick sputtered $Ni_{1-x}Fe_x$ metal; ∼7 nm thick electrodeposited $Ni_{1-x}Fe_x(OH)_2$ assuming a total film density that is a weighted average of the constituents $Ni(OH)_2$ and $Fe(OH)_2$, 4.1 and 3.4 g cm^{-3}, respectively). Film thicknesses of ∼2 nm were targeted to ensure the sputtered metallic films fully converted to the (oxy)hydroxide phase, confirmed via XPS after electrochemical characterization and by integrating the Ni redox peak areas. (For example, 3.1−3.7 × 10^{15} electrons are transferred during the reduction of NiOOH to $Ni(OH)_2$ for a sputtered Ni film, which is comparable to the target value of Ni atoms sputtered.)

Films were electrodeposited with a cathodic current density of −50 μA cm^{-2} for 113 s using solutions of nickel sulfate hexahydrate (≥99.99% trace metals basis, Sigma-Aldrich 467901) and iron sulfate heptahydrate (ACS Reagent ≥99.0%, Sigma-Aldrich 215422). Preparation of nickel and iron sulfate deposition solutions is detailed in our previous work (concentrations of deposition solutions with resulting Fe compositions are detailed in Supporting Information S2), along with estimations of the film thicknesses as determined by inductively coupled plasma optical emission spectroscopy (ICP-OES).[24] We note that different nomenclature is used to distinguish target and measured compositions. For example, a 50% Fe target composition is noted as x = 0.5, while a 50% Fe composition determined via XPS is notated as $Ni_{0.5}Fe_{0.5}$.

Sputter depositions were carried out using an AJA International ATC Orion 5 sputtering instrument. $Ni_{1-x}Fe_x$ films were obtained by cosputtering two separate metallic Ni and Fe targets (Kurt Lesker, 99.9% Ni and 99.95% Fe, 2 in. diameter). DC and RF power supplies were used for Ni and Fe, respectively. Typical powers ranged from 15 to 107 W for Ni and 29 to 200 W for Fe. This enabled preparation of mixed $Ni_{1-x}Fe_x$ films with Fe contents of $0.05 \leq x \leq 0.95$. Total deposition rates ranged between 0.04 and 0.08 nm s^{-1}, depending on the targeted film composition (see the Supporting Information for deposition parameters). The base pressure in the deposition chamber was below 1 × 10^{-7} Torr prior to deposition, and depositions were carried out at room temperature under an atmosphere of 15 mTorr Ar. An aluminum shadow mask was used to confine the deposition area to the 5 mm diameter gold electrode. The rates and compositions were estimated via individual rate calibrations with an internal quartz crystal microbalance and verified by ICP-OES (Supporting Information). In the case of layered films, the deposition parameters were identical to those for mixed films of the same overall composition, except that the shutters were controlled to enable sequentially deposited elemental layers.

Since $Ni_{1-x}Fe_x$ films prepared by sputter deposition are metallic, they require electrochemical conversion to the $Ni_{1-x}Fe_xOOH$ catalytic phase in KOH. Although only the sputtered films require electrochemical conversion to the (oxy)hydroxide, for consistency, *both* sputtered *and* electrodeposited films were cycled between 0.0 and 0.7 V vs Hg/HgO at 10 mV s^{-1} in 0.1 M KOH for the same duration (14−16 h) prior to electrochemical characterization. Representative voltammograms collected throughout this cycling "stabilization" process for sputtered and electrodeposited films can be found in the Supporting Information.

2.2. Electrochemical Characterization. $Ni_{1-x}Fe_x$ films with $x \leq 0.90$ were characterized in "Fe-free" KOH. For films with $x > 0.90$, commercial KOH (prepared from Baker Analyzed Electronic grade KOH solution, VWR JT3144-3) was used as the electrolyte, since after the electrolyte cleaning process, the purified Fe-free electrolyte is expected to contain low-levels of $Ni(OH)_2$ impurities that may alter the film

DOI: 10.1021/acs.jpcc.5b04776
J. Phys. Chem. C 2015, 119, 18303−18316

composition during electrochemical characterization. The uncompensated series resistance iR_u was determined by potentiostatic electrochemical impedance spectroscopy, and the measured ohmic resistance value was internally compensated at 95%. Cyclic voltammograms were collected at 10 mV s^{-1}. For chronopotentiometric experiments, the full iR_u value was corrected manually during data analysis. For rotating-disk electrode (RDE) experiments, a rotation rate of 1600 rpm was used. All electrochemical measurements were carried out in a glass-free environment to prevent etching of glass components by the caustic electrolyte, which can introduce Fe and other impurities into the solution. All potentials are reported vs a Hg/HgO reference electrode (CH Instruments) filled with 1 M KOH. The equilibrium potential for the oxygen evolution reaction 0.1 M KOH (pH 13) is 0.365 V vs the Hg/HgO reference. A coiled Pt wire served as the counter electrode (99.95%, DOE BCPMSR) and was placed within a porous polypropylene compartment inside the electrochemical cell. The Pt counter electrodes were periodically cleaned by overnight soaking in 1 M H_2SO_4.

2.3. In Situ Raman Spectroscopy. Raman spectra were collected using a confocal Raman microscope (LabRAM HR, Horiba Yvon Jobin) with an excitation wavelength of 633 nm. The power was ~1.5 mW at the sample surface and the spot size of the laser beam is estimated to be between 1 and 2 μm. Acquisition times were typically 3 s and the spectral resolution is ~1 cm^{-1} with a 600 mm^{-1} grating. Spectral shifts were calibrated using the silicon phonon mode (520.7 cm^{-1}) of a silicon wafer. High wavenumber spectra were background subtracted in the instrument software (Labspec) to more clearly show features in this region.

In situ Raman spectra were collected for catalyst films of select compositions under controlled electrochemical potentials using a homemade cell fabricated from Teflon. The cell contained a Teflon-sheathed gold working electrode (5 mm diameter) oriented at the bottom of the cell. We employed a water-immersion objective (70× mag., NA = 1.23, LOMO) which was protected from the corrosive KOH electrolyte by a 0.0005″ thick Teflon film (American Durafilm). A droplet of water was placed between the objective lens and the film to retain high illumination/collection efficiencies.

Electrodeposited films were prepared on working electrodes in a Teflon cell, while sputter-deposited films were prepared using aluminum shadow masks which confined the deposition of the film to the exposed gold working electrode. All films were cycled for 15 h prior to characterization by Raman spectroscopy. Raman spectra were collected as the potential of the working electrode was scanned at a rate of 1 mV s^{-1}. A Hg/HgO (filled with 1 M KOH) reference electrode and a Pt wire counter electrode were used for electrochemical Raman experiments, and all experiments were performed in 0.1 M KOH electrolyte at room temperature.

2.4. X-ray Photoelectron Spectroscopy. X-ray photoelectron spectra were collected with a Kratos Axis Ultra spectrometer using a nonmonochromatic Mg Kα source (10 mA, 15 kV). The Al Kα source was not used due to the presence of Ni LMM Auger features overlapping with the Fe $2p_{3/2}$ peak. The base pressure in the analytical chamber was ~7 × 10^{-9} Torr. Spectra shown in this work (Ni 2p, Fe 2p, O 1s, Au 4f, C 1s) were collected with a pass energy of 20 eV and a step energy of 50 meV. The Fe 2p and Ni 2p regions were collected using dwell times of 300−500 ms and were averages of 5−10 scans to obtain high spectral signal-to-noise. The composition (by metal content) was estimated using relative sensitivity factors of 21.1, 16.0, and 17.4 for Ni 2p, Fe 2p, and Au 4f, respectively. A Shirley background was used for the Ni 2p region, and a Shirley or linear background was used for the Fe 2p region to accommodate the rising background from an oxygen Auger feature (O KLL) with an onset binding energy near 732 eV. (See the Supporting Information for representative spectra with background fits.) The Au 4f spectrum for the underlying gold substrate (Au $4f_{7/2}$ at 84.0 eV)[25] was used for spectral charge-shift calibration. Angle-resolved X-ray photoelectron spectroscopy (XPS) measurements were carried out by varying the electron takeoff angle between 0° and 70° with respect to the sample normal. All spectra were analyzed using CasaXPS (Casa Software, Ltd.).

3. RESULTS AND DISCUSSION

3.1. Comparison of Codeposited $Ni_{1-x}Fe_xOOH$ Films Prepared by Sputter Deposition and Electrodeposition. *3.1.1. Effects of Stabilization Cycling and Electrochemical Characterization on Film Composition.* To check compositional stability of both sputter-deposited and electrodeposited samples, Fe content was determined for x = 0.25 and x = 0.50 films prepared by each deposition method as-deposited and after completion of all electrochemical treatments (stabilization CV cycling followed by characterization). As shown in Table 1,

Table 1. Comparison of Fe Contents As Determined by XPS Before (As-Deposited) and After Electrochemical Stabilization and Characterization for Select $Ni_{1-x}Fe_x$ Films

sample type	as-deposited [mol % Fe]	after electrochemical stabilization [mol % Fe]	after electrochemical characterization [mol % Fe]
x = 0.25 electrodeposited	28%	n/a	30%
x = 0.50 electrodeposited	56%	n/a	44%
x = 0.25 sputter-deposited	25%	15%	14%
x = 0.50 sputter-deposited	52%	30%	29%

the x = 0.25 electrodeposited sample displayed no clear loss of Fe after electrochemical stabilization and characterization, while the x = 0.50 electrodeposited sample exhibits a small reduction in Fe content (56% Fe as-deposited vs 44% Fe, with % Fe given as the percent of total metals [Ni + Fe] as determined via XPS).

In contrast, significant Fe loss is observed for both sputter-deposited samples after electrochemical stabilization and characterization. The sample with x = 0.25 was determined to contain 14% Fe, while the x = 0.50 sample contained 29% Fe. To determine if the Fe/Ni ratio is changing during the 15 h stabilization cycling or during electrochemical characterization, the Fe contents of sputtered films were also determined after 15 h of stabilization cycling but before electrochemical characterization. For both x = 0.25 and x = 0.50 sputtered films, the Fe contents (~15% and ~30% Fe, respectively) were similar after stabilization cycling vs after electrochemical characterization.

From these results (as well as the angle-resolved XPS measurements discussed in subsection 3.2), it is clear that a significant amount of Fe is lost from the sputtered films when the films convert from as-deposited metal to metal oxide/hydroxide during stabilization cycling. However, once this

DOI: 10.1021/acs.jpcc.5b04776
J. Phys. Chem. C 2015, 119, 18303−18316

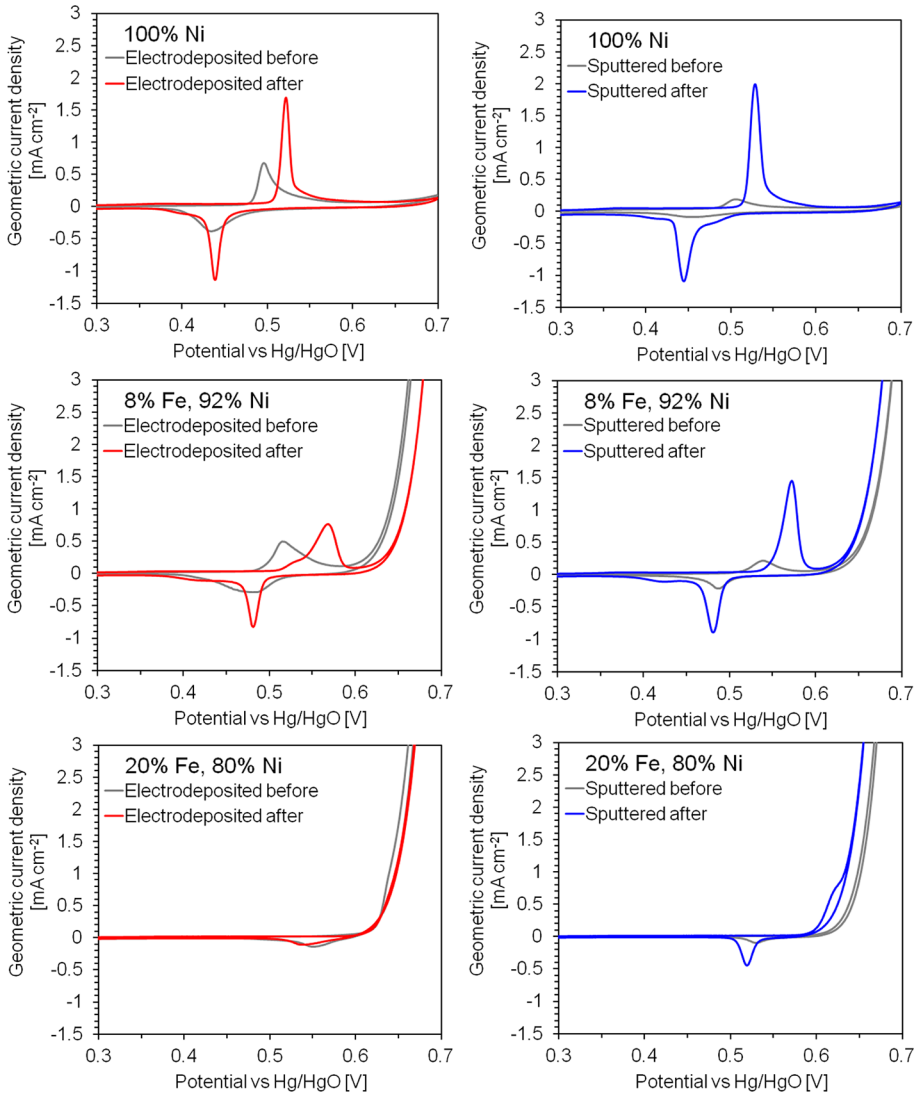

Figure 1. Cyclic voltammograms of $Ni_{1-x}Fe_x(OH)_2$/$Ni_{1-x}Fe_xOOH$ films for both electrodeposited (left) and sputtered (right) films, showing the change in voltammetry as-deposited (before, gray) and after stabilization and electrochemical characterization (red, blue). CVs were collected in 0.1 M KOH at 10 mV s^{-1}.

transformation is complete, the relative Fe contents remain stable during electrochemical characterization (i.e., under oxygen evolution conditions). We observed Fe loss during stabilization for sputtered films with target compositions of $0.25 \leq x \leq 0.75$ (Table S2.1). Therefore, all further comparisons are made using % Fe contents determined by XPS after electrochemical characterization.

3.1.2. Effects of Electrochemical Stabilization on Voltammetry. Figure 1 shows voltammograms of electrodeposited and sputtered films with 0%, 8%, and 20% Fe, shown at the beginning of stabilization (gray, second stabilization cycle) and after electrochemical characterization (red and blue). For pure Ni films, a significant amount of Ni is found to further convert from metal to (oxy)hydroxide during the OER activity measurements, as evidenced by an increase in the area under the Ni redox waves[26,27] (Figure S3.2). However, despite the change in redox peak, only minimal improvement in OER activity is observed, consistent with recent observation that Fe-free NiOOH is a very poor OER catalyst.[23]

Films prepared by both deposition methods show qualitatively similar electrochemical behavior and exhibit features characteristic of $Ni_{1-x}Fe_xOOH$,[13−17,22−24,28] specifically a redox couple in the range of 0.40−0.63 V corresponding to the oxidation/reduction of Ni in $Ni(OH)_2$/NiOOH and an increase in current density at higher potentials due to the electrocatalytic oxidation of water. As reported in our previous work,[24] the positions and intensities of both features depend on the composition of the films. Specifically, the $Ni(OH)_2$/NiOOH redox peaks shift to higher potentials with increasing Fe content, and the OER current densities are the lowest for pure Ni and pure Fe films and highest for intermediate Fe contents. (In addition, features associated with reversible oxidation and reduction of the underlying Au substrate can be observed for some samples at ∼0.36 and ∼0.24 V vs Hg/HgO, respectively.)

Despite these general similarities, notable differences exist between the electrochemical characteristics of sputtered and electrodeposited films. Sputtered films containing Ni initially show smaller Ni redox peaks, with the Ni oxidation wave almost not visible for samples with sufficiently high Fe contents (e.g., 20% Fe). With repeated cycling, there is a significant growth in the total area under the redox features (the integrated

DOI: 10.1021/acs.jpcc.5b04776
J. Phys. Chem. C 2015, 119, 18303−18316

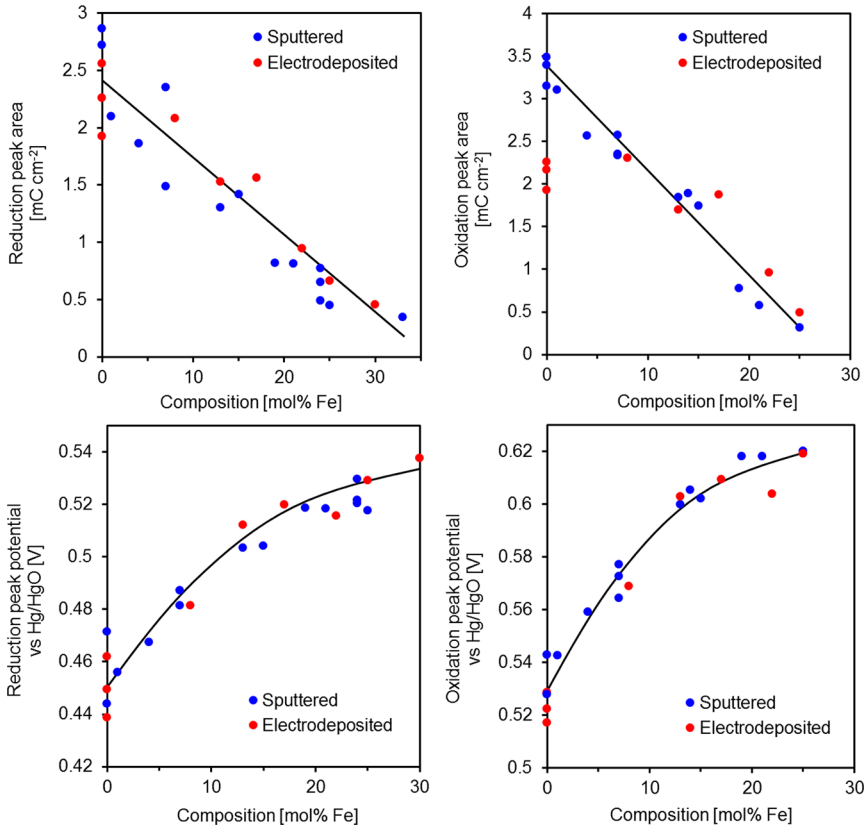

Figure 2. Comparison of redox characteristics for sputtered (blue) and electrodeposited (red) $Ni_{1-x}Fe_x(OH)_2/Ni_{1-x}Fe_xOOH$ films. Oxidation and reduction peak areas (top) and potentials (bottom) are plotted as a function of Fe content. Values were obtained from fitting the redox peaks in cyclic voltammograms measured in 0.1 M KOH after electrochemical activity measurements, with a scan rate of 10 mV s^{-1} and a rotation speed of 1600 rpm. Curves are included to guide the eye.

area of the oxidation wave for the 20% Fe sample increases more than 3-fold, from 0.39 to 1.4 mC cm^{-2}), stabilizing after ~300 cycles. On the other hand, electrodeposited films are predominantly deposited as oxides/hydroxides (further discussion detailed in subsection 3.1.6) and do not exhibit the same behavior. $Ni_{1-x}Fe_x(OH)_2$ electrodeposited films exhibit minimal changes in the reduction peak areas after extended cycling (e.g., the reduction wave for the 20% Fe sample is comparable after deposition vs after stabilization: 1.47 vs 1.42 mC cm^{-2}). Additionally, the voltammograms for sputtered films display sharper redox peaks than those for electrodeposited films, indicating greater uniformity in sputtered films compared to electrodeposited films. With the exception of pure Ni (for which no significant OER current is observed up to 0.7 V vs Hg/HgO), sputtered films tended to show an increase in OER activity after cycling, while electrodeposited films displayed a slight decrease or negligible change in activity.

Figure 2 shows a comparison of the Ni reduction/oxidation peak positions and areas for electrodeposited and sputtered films with ~30% Fe or less after electrochemical characterization. (For film compositions exceeding 30% Fe, oxidation waves become increasingly difficult to fit and analyze due to overlap with oxygen evolution currents. Representative peak fits are shown in the Supporting Information, S3.1.) Within sample-to-sample variation (across different samples of the same composition), the redox areas and peak positions are comparable, apart from the oxidation peak area of 100% Ni, for which sputtered Ni shows a larger oxidation peak area compared to electrodeposited Ni. Despite the qualitative differences in the peak shape discussed above, this analysis shows that the amount of redox-accessible material is comparable for any given $Ni_{1-x}Fe_x(OH)_2/Ni_{1-x}Fe_xOOH$ film composition, regardless of the film deposition method.

3.1.3. Comparison of OER Activity and Turnover Frequency for Stabilized Films. The activity for the OER was quantified using (1) the overpotential, η, at a geometric current density of 10 mA cm^{-2} and (2) the geometric current density, j, at η = 300 mV, each after holding for 1 h at the specified condition. These two metrics are plotted for both sputtered and electrodeposited films in Figure 3. Within sample-to-sample variation, the activities of electrodeposited and sputtered films of any given composition are comparable. The overpotential reaches a minimum of ~320 mV at 15−20% Fe, compared to overpotentials as high as 750 mV for Ni and 500 mV for Fe. Likewise, the current density varies by approximately three orders of magnitude across the entire composition range, reaching a maximum of ~3 mA cm^{-2} for ~15−20% Fe, and with minima on the order of $j = 1 \times 10$ mA cm^{-2} for NiOOH or FeOOH. The composition with the maximum OER activity observed here is well within the range measured in previous studies, between 10 and 50% Fe.[15,16,24,28] We note the electrodeposited films reported here exhibit 10× lower current density at 300 mV overpotential than those reported in previous work from our group,[24] coinciding with a 10× decrease in catalyst loading (~3.5×10^{15} atoms deposited in the current study vs ~3.5×10^{16} atoms deposited previously). This difference could be due to differences in the real vs geometric surface area or a greater number of active sites

DOI: 10.1021/acs.jpcc.5b04776
J. Phys. Chem. C 2015, 119, 18303−18316

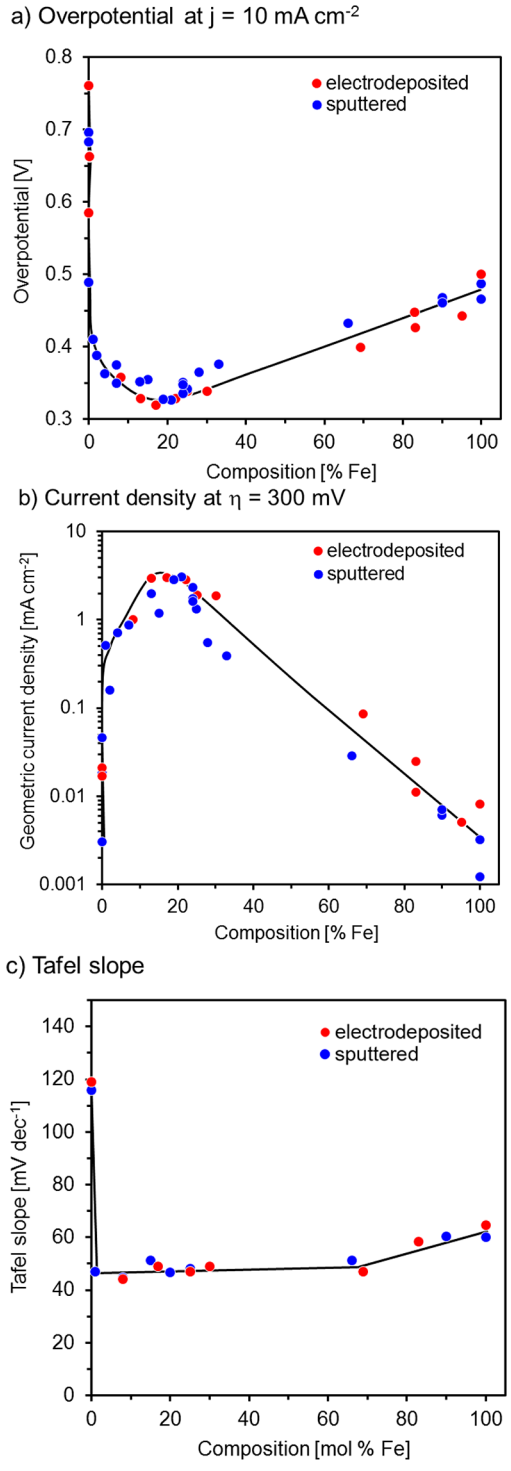

Figure 3. Activity plots for sputtered and electrodeposited $Ni_{1-x}Fe_xOOH$ films. Activity values were obtained after holding for 1 h at either constant (a) geometric current density (10 mA cm^{-2}), (b) overpotential (300 mV), or with (c) Tafel slopes obtained from 10 mV s^{-1} CV scans. Measurements were obtained in 0.1 M KOH with a RDE rotation rate of 1600 rpm. Curves are included to guide the eye.

due to the electrolyte/ion permeability of Ni-based (oxy)-hydroxides.[23,29−31]

Tafel slope values are shown in Figure 3c (with slope fits shown in the Supporting Information, S3.5). Both sputtered and electrodeposited NiOOH exhibit comparable Tafel slopes to those previously reported for Fe-free NiOOH (115−120 mV dec^{-1}).[29] With even a 1% addition of Fe, a substantial decrease in the Tafel slope (and increase in activity) is observed, consistent with the enhancement in OER activity observed over NiOOH after incorporation of ppb-level Fe impurities.[23,29] Tafel slopes for $Ni_{1-x}Fe_xOOH$ are ∼45−50 mV dec^{-1}, in agreement with Tafel slopes measured for other Ni−Fe(oxy)-hydroxide electrocatalysts (40−50 mV dec^{-1}).[24,32−34] As Fe content increases above 75%, an increase in Tafel slopes to ∼64 and ∼60 mV dec^{-1} is observed for electrodeposited and sputtered 100% Fe films, respectively. Previous work has shown a higher Tafel slope for pure Fe (∼55 mV dec^{-1}) vs those for $Ni_{1-x}Fe_xOOH$ films.[24]

Note that in the case of sputtered films, the increase in OER current does not appear to be proportional to the change in Ni redox peak areas. For example, for the sputtered film with 20% Fe, the reduction peak area increases by more than 3-fold, while the OER current (at 665 mV vs Hg/HgO, or 300 mV overpotential) increases by less than 2-fold (2.8 to 5.2 mA cm^{-2}). Similarly, for sputtered films with 8% Fe, the reduction peak area increases by almost 4-fold (0.6 to 2.1 mC cm^{-2}) while the OER current density increases by less than 2-fold (0.78 to 1.4 mA cm^{-2}). This suggests that not all (if any) of the electrochemically accessible (i.e., redox-active) Ni population is participating in OER catalysis. This is consistent with recent work for Ni- and Co-(oxy)hydroxide thin films indicating the Fe atoms as the actual OER active sites.[35,36] A further discussion of Fe as the OER-active site is presented in the Supporting Information, S3.6.

3.1.4. Long-Term Stability Comparison of Sputtered and Electrodeposited Films with 20% Fe. Previous work investigating sputter-deposited Fe-doped NiO_x films found a greater long-term stability (i.e., catalyst did not separate from the substrate) of sputtered films relative to electrodeposited films during oxygen evolution.[22] This stability increase was attributed to better adhesion of the sputtered Fe/NiO_x film to the underlying Ni substrate. To further investigate effects of deposition method on catalyst stability, we measured oxygen evolution activity on both a short-term (1 h) and long-term (38 h) basis. After 1 h at 10 mA cm^{-2} (anodic), electrodeposited films with ∼20% Fe exhibited a ∼9 mV increase in overpotential (670−679 mV) compared to a 3−4 mV increase in overpotential for 20% Fe (stabilized) sputter-deposited films. To test the long-term stability of electrodeposited vs sputtered films, 20% Fe films produced by both depositions were held at a 10 mA cm^{-2} current density for 38 h. Cyclic voltammograms for each film before and after 38 h of oxygen evolution are shown in Figure 4. The sputtered film initially exhibits higher OER current compared to the electrodeposited film at potentials above 0.7 V. However, after 38 h of sustained oxygen evolution, the CV of the electrodeposited film is largely unchanged, while a loss in activity is apparent for the sputtered film.

Additional activity and composition comparisons are shown in Table 2. Even after 6 h at j = 10 mA cm^{-2}, comparable overpotentials are observed for the electrodeposited (327 mV) and sputter-deposited (325 mV) films with 20% Fe. After 38 h of oxygen evolution, however, the electrodeposited film exhibited a lower overpotential (317 mV), while the sputtered film showed a slight increase in overpotential (334 mV). The Fe content of each film was also determined after 38 h of sustained oxygen evolution using XPS; the electrodeposited film contained 18% Fe (close to the 20% Fe targeted), while the sputter-deposited sample exhibited significant Fe loss, with

DOI: 10.1021/acs.jpcc.5b04776
J. Phys. Chem. C 2015, 119, 18303−18316

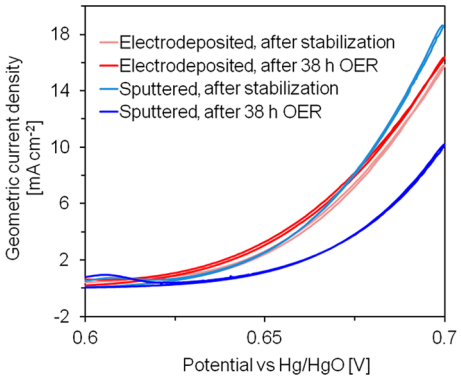

Figure 4. Cyclic voltammograms of films with 20% Fe deposited by sputtering (blue) and electrodeposition (red) after electrochemical stabilization cycling and after 38 h at a geometric current density of 10 mA cm^{-2}. CVs were collected on RDEs with a rotation rate of 1600 rpm and scan rate 10 mV s^{-1} in 0.1 M KOH.

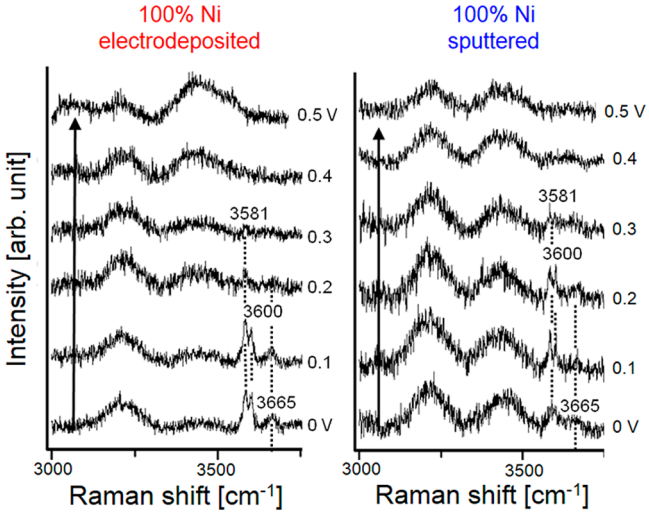

Figure 5. High-wavenumber in situ Raman spectra for 100% Ni electrodeposited and sputter-deposited on roughened Au substrates as a function of potential vs Hg/HgO in 0.1 M Fe-free KOH, for which the OER equilibrium potential is 0.365 V.

only 13% Fe remaining in the film after sustained oxygen evolution. The loss of Fe and activity of the sputtered $Ni_{1-x}Fe_xOOH$ film cannot be due to complete degradation of the film, since the Ni reduction peak area of the sputtered sample significantly increases (rather than decreasing as would be expected with film dissolution) during the 38 h of sustained oxygen evolution. (We use this metric to evaluate film stability since the 2 nm $Ni_{1-x}Fe_xOOH$ film is too thin for accurate quantification of total metal content by ICP-OES.) In summary, both sputter-deposited and electrodeposited films demonstrate high activity and stability for the OER, though the sputtered films exhibit some loss of Fe and a slight decrease in activity after 38 h of oxygen evolution.

3.1.5. In Situ Raman Spectroscopy of $Ni_{1-x}Fe_xOOH$ After Electrochemical Stabilization. To further investigate structural differences between electrodeposited and sputter-deposited films, in situ Raman spectra were obtained for $Ni_{1-x}Fe_xOOH$ films of select compositions (100% Ni, 25% Fe and 100% Fe). Spectra were collected during a 1 mV s^{-1} oxidation sweep (from 0.00 to 0.65 V vs Hg/HgO) in 0.1 M KOH after electrochemical stabilization (corresponding voltammograms are presented in the Supporting Information, S5). For all three compositions, Raman spectra for the electrodeposited and sputter-deposited samples are similar, indicating comparable structures exist between the corresponding compositions of sputtered and electrodeposited films.

Figure 5 shows the Raman spectra acquired in the high-wavenumber (3000−3800 cm^{-1}) O−H stretching regime for sputter-deposited and electrodeposited 100% Ni films. Both sputter-deposited and electrodeposited 100% Ni films exhibit three Raman modes at 3581, 3600, and 3665 cm^{-1} between 0.0 to 0.2 V. The Raman feature present at 3665 cm^{-1} is characteristic of α-$Ni(OH)_2$, while the feature at 3581 cm^{-1} is attributed to β-$Ni(OH)_2$.[26,37−40] Additionally, the 3600 cm^{-1} peak corresponds to a stacking fault disorder within the β-$Ni(OH)_2$ phase.[40] With oxidation to 0.3 V, however, only a weak feature at 3581 cm^{-1} is observed due to the phase conversion of $Ni(OH)_2$ to NiOOH with the anodic potential scan. These results suggest that the $Ni(OH)_2$ phase is best described as a mixture of α-$Ni(OH)_2$ and disordered β-$Ni(OH)_2$, consistent with our previous observations over similar films.[24] In contrast, none of the O−H stretching modes of either the α- or β-$Ni(OH)_2$ phases were observed for the 25% and 100% Fe films (SI, S5), consistent with previous studies showing these features are not observable for electrodeposited films with >19% Fe codeposition or after Fe electrolyte impurity incorporation into the $Ni(OH)_2$ structure.[24,29] Apart from the Raman features ascribed to $Ni(OH)_2$, only contributions due to bulk water modes from 3100 to 3600 cm^{-1} are observed,[26,40,41] which are present in the spectra of all samples.

Raman spectra acquired at low wavenumbers (200−800 cm^{-1}) for 100% Fe, 25% Fe, and 100% Ni are presented in Figure 6. The Raman spectra of 100% Fe films for both sputter-deposited and electrodeposited contain no discernible features apart from a weak ∼580 cm^{-1} contribution above 0.4 V due to electrochemical oxidation of the underlying Au substrate.[42] The absence of other spectral features for the Fe samples, an incongruity with our previous investigation, is attributed to the 10-fold film thickness decrease in the present study (previous 25 nm vs current 2.5 nm estimated thickness over roughened Au electrodes).[24]

For electrodeposited and sputter-deposited 100% Ni films, a weak Raman feature at 493 cm^{-1} is initially observed at 0.1 V vs Hg/HgO. This feature is attributed to a defective or disordered $Ni(OH)_2$ structure.[24,26,43] Features at ∼480 and 560 cm^{-1}, characteristic of NiOOH,[24,38,44] appear at 0.4 V and intensify

Table 2. Comparison of Overpotential at 10 mA cm^{-2}, Composition, and Reduction Peak Area Change for Stabilized 20% Fe Sputter-Deposited and Electrodeposited Films

	overpotential after 1 h [mV]	overpotential after 6 h [mV]	overpotential after 38 h [mV]	surface composition after 38 h [mol % Fe]	Reduction peak area change [% increase]
electrodeposited	314	327	317	18%	7%
sputter-deposited	317	325	334	13%	28%

DOI: 10.1021/acs.jpcc.5b04776
J. Phys. Chem. C 2015, 119, 18303−18316

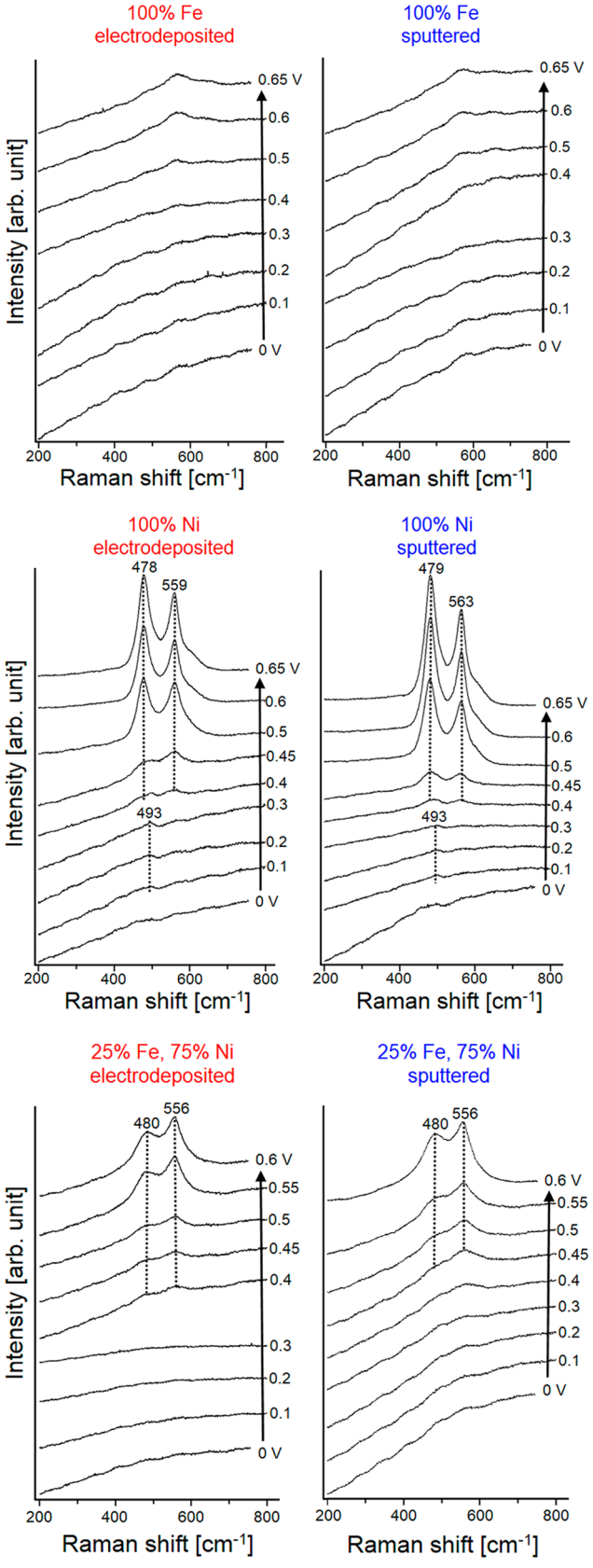

Figure 6. Low-wavenumber in situ Raman spectra for 100% Fe, 100% Ni, and 25% Fe films electrodeposited and sputter-deposited on roughened Au substrates as a function of potential vs Hg/HgO in 0.1 M Fe-free KOH, for which the OER equilibrium potential is 0.365 V.

most greatly from 0.45 to 0.5 V, coinciding with the $Ni(OH)_2$/NiOOH oxidation wave within the voltammograms (Figure S5.1) for both samples. The sputter-deposited 100% Ni film exhibits sharper, more defined NiOOH features, indicating greater structural order within this film. Note that this is consistent with the observation of sharper Ni redox features in cyclic voltammograms of sputtered films in comparison to electrodeposited films.

For the 25% Fe films, several differences compared to 100% Ni films indicate the presence of Fe within the $Ni(OH)_2$/NiOOH structure. While the 480 and 560 cm^{-1} features are also present for these samples at 0.4 V and above, these peaks exhibit weaker intensities and a lower 480 cm^{-1} to 560 cm^{-1} peak height ratio. Such differences are consistent with reports of an oxidized Ni−Fe layered double hydroxide structure.[29,45] Additionally, the 480 and 560 cm^{-1} Raman features intensify most strongly when the potential increases from 0.50 to 0.55 V, a 0.05 V anodic shift in comparison to the 100% Ni films (0.45−0.50 V). This delayed onset of oxyhydroxide formation coincides with the anodic shift of the Ni oxidation wave observed in the corresponding voltammograms, indicating Fe incorporation into the Ni structure.[24,29]

In summary, in situ Raman spectra show clearly that minimal structural differences exist between $Ni_{1-x}Fe_xOOH$ films prepared by sputter deposition and electrodeposition. It should be noted that films deposited via both methods exhibit structural disorder, as indicated by the presence of the 490 and 3600 cm^{-1} features for the 100% Ni films, as well as the absence of Raman features for the pure Fe films. This finding is consistent with previous in situ Raman and X-ray diffraction studies of electrodeposited nickel−iron hydroxides, which also observed disordered structures for $Ni_{1-x}Fe_xOOH$.[22,23,39]

3.1.6. X-ray Photoelectron Spectroscopy of Films As-Deposited and after Electrochemical Characterization. Conversion of the sputtered $Ni_{1-x}Fe_x$ metallic films to the (oxy)hydroxides after extended cycling was also confirmed via XPS. The Ni 2p, Fe 2p, and O 1s spectra for sputtered and electrodeposited $x = 0.25$ (as-deposited composition) films are shown in Figure 7. Ni is initially present as metal (870.0 and 852.6 eV) and NiO (856.0/861.4 eV Ni $2p_{3/2}$, 873.5/879.3 eV Ni $2p_{1/2}$) in the as-sputtered film,[25,46] but only peaks consistent with a nickel (oxy)hydroxide phase are observed after electrochemical characterization (856.3/862.0 eV Ni $2p_{3/2}$, 874.0/880.0 eV Ni $2p_{1/2}$).[25,46] The Fe 2p spectrum for the as-sputtered $Ni_{0.75}Fe_{0.25}$ film exhibits peaks at 707.0 and 719.8 eV, attributed to metallic Fe,[25,47] while the remaining peaks (724.0 and 710.9 eV) are attributed to iron oxide or hydroxide phases.[47] The specific phase of iron oxide/hydroxide cannot be uniquely identified due to similarities in the Fe 2p binding energies and spectral shapes of the higher oxides of iron and limitations in the spectral line resolution with the non-monochromated Mg Kα source. The O 1s spectrum for the as-sputtered film displays two peaks due to unprotonated oxygen (~530 eV) and protonated oxygen (~531.5 eV), while after characterization, only one peak at 531.5 eV is observed.

The Ni 2p spectra for the as-electrodeposited $Ni_{0.75}Fe_{0.25}(OH)_2$ film exhibits peaks consistent with nickel hydroxide (855.6/861.4 eV Ni $2p_{3/2}$, 873.3/880 eV Ni $2p_{1/2}$).[25,46] Additionally, a peak observed at 852.8 eV is consistent with metallic Ni. After electrochemical stabilization and characterization, peaks again consistent with a nickel (oxy)hydroxide are observed (856.1/861.9 eV Ni $2p_{3/2}$, 873.9/880 eV Ni $2p_{1/2}$ region). The as-electrodeposited

DOI: 10.1021/acs.jpcc.5b04776
J. Phys. Chem. C 2015, 119, 18303−18316

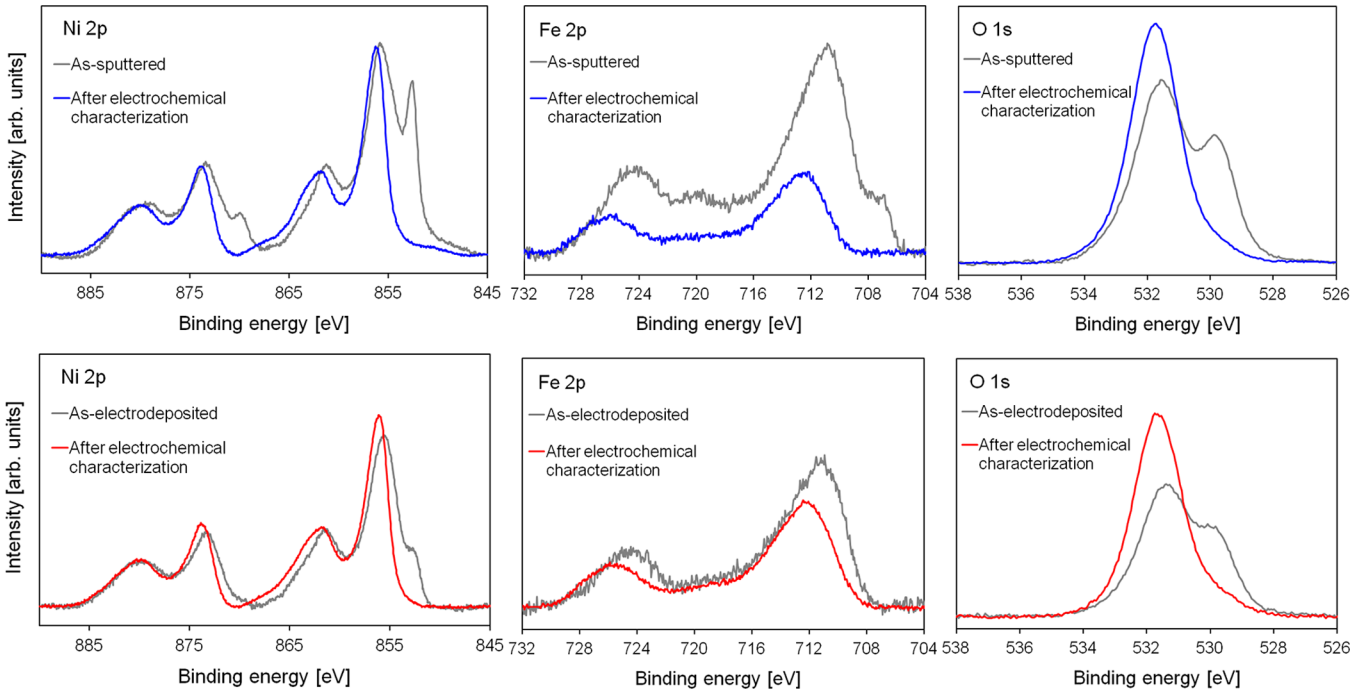

Figure 7. Comparison of Ni 2p, Fe 2p and O 1s XPS spectra (background-subtracted) for sputtered and electrodeposited films with target compositions x = 0.25, as-deposited (gray) and after electrochemical stabilization and characterization (blue, red).

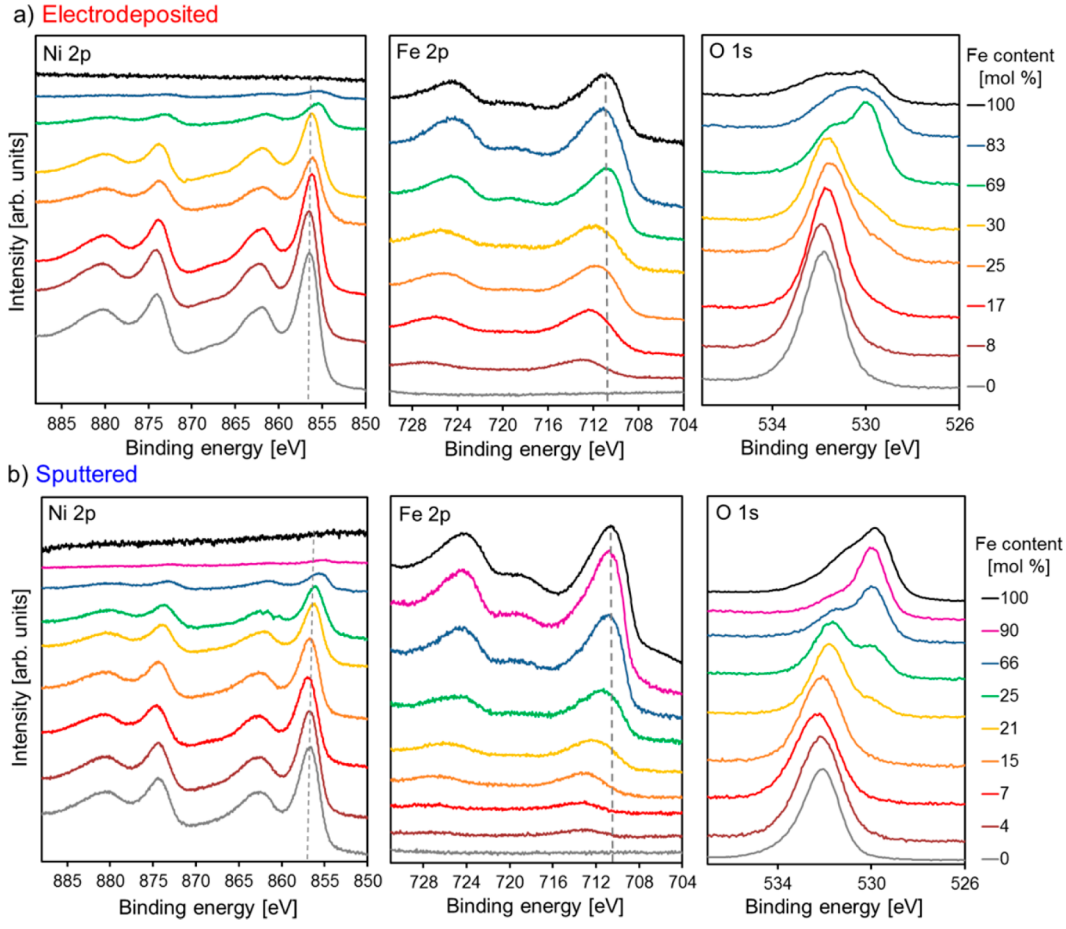

Figure 8. Comparison of Ni 2p, Fe 2p, and O 1s XPS spectra (charge-corrected) for (a) electrodeposited and (b) sputtered films after electrochemical characterization. Gray dashed lines (at 710.7 and 856.6 eV for Fe and Ni, respectively) are shown for pure Fe and Ni peak positions for reference. Fe contents are those determined by XPS after electrochemical stabilization and characterization.

DOI: 10.1021/acs.jpcc.5b04776
J. Phys. Chem. C 2015, 119, 18303−18316

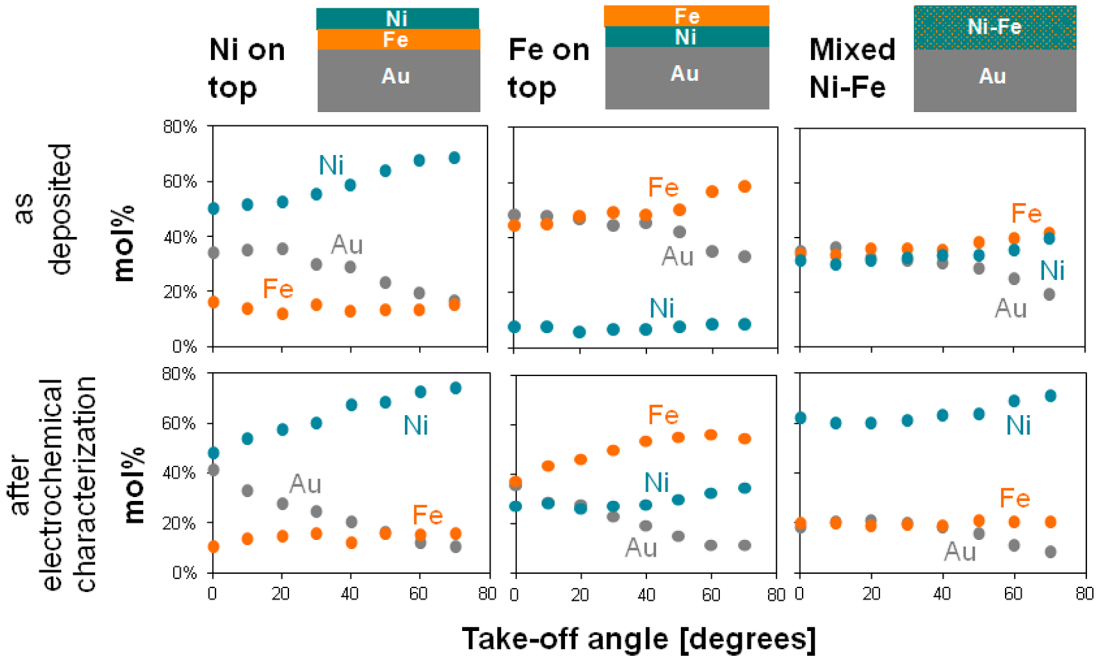

Figure 9. Depth profiles obtained from Ni 2p, Fe 2p and Au 4f XPS spectra for films as-deposited (sputtered) and after electrochemical characterization for Ni-on-top, Fe-on-top, and mixed Ni−Fe samples (50:50 Fe/Ni).

$Ni_{0.75}Fe_{0.25}(OH)_2$ film exhibits a Fe 2p spectrum with peaks at 711.1 and 724.3 eV, again consistent with Fe oxide/hydroxide phases. (No contribution from metallic Fe is observed.) The as-electrodeposited sample also exhibits O 1s spectral features consistent with both protonated and unprotonated oxygen (at 530.1 and 531.5 eV) in the O 1s region, while after characterization, only a protonated oxygen contribution (~531.6 eV) is present.

Figure 8 compares the XPS spectra of electrodeposited (Figure 8a) and sputtered (Figure 8b) films after electrochemical characterization. The Ni 2p peaks shift to slightly lower binding energies for films with Fe contents of 66% and above but remain otherwise unchanged. For sputtered and electrodeposited films with Fe contents of 25−30% and below, the Fe 2p binding energy increases between ~1.0−2.0 eV. While no previous XPS studies have detailed the differences in binding energy for Fe present as $Ni_{1-x}Fe_xOOH$, Fe present in an oxyhydroxide has been reported to exhibit similar Fe 2p and O 1s spectra to the low Fe content films reported here.[48] Additionally, the ~530 eV O 1s peak observed in the spectra of 100% Fe films is not observed for films with Fe contents below ~25% (electrodeposited) and ~31% (sputter-deposited). Instead, the O 1s spectra of films with low Fe-contents (~15−17% Fe and below) exhibit only one primary O 1s peak at ~531.6 eV, consistent with a protonated oxygen,[25,48] which may be bound to Ni and/or Fe.

The presence of one primary O 1s peak below ~20% Fe indicates that a single phase predominates after electrochemical stabilization/characterization of sputtered and electrodeposited $Ni_{1-x}Fe_xOOH$, which appears characteristic of a Ni(oxy)-hydroxide-type structure. This finding is consistent with the in situ Raman spectra in Figure 6, as well as previous reports from our group, which found that Fe can incorporate into the $Ni(OH)_2$/NiOOH structure for Fe contents below 25%.[29,35] In our current study, we find that a separate, Fe-rich phase (characteristic of pure Fe oxide/hydroxide) is first observable (evidenced most clearly by the observation of an additional O 1s peak) between 17% and 25% Fe contents for sputtered films and between 15 and 21% Fe contents for electrodeposited films.

In summary, spectroscopic evidence suggests a single $Ni_{1-x}Fe_xOOH$ phase predominates below 20 mol % Fe after electrochemical characterization for both sputtered and electrodeposited films. As Fe content increases above 20%, the formation of a Fe-rich phase and a decrease in OER activity is observed. This further supports our previous hypothesis that Fe is the active site for oxygen evolution and that the decrease in activity for catalyst films with Fe contents in excess of 20% is due to the formation of a separate, Fe-rich phase.[29,35] It is possible that such a phase is less OER-active due to low electrical conductivity, which has been previously reported for FeOOH under oxygen-evolving potentials in alkaline electrolyte,[36] and/or due to less optimal binding energetics of OER-intermediates relative to Fe within a Ni (oxy)hydroxide structure.[35]

3.2. Comparison of Codeposited and Layered $Ni_{1-x}Fe_x$ Films. In the previous section, we demonstrated that $Ni_{1-x}Fe_xOOH$ catalysts prepared by sputter deposition and electrodeposition are essentially identical with respect to activity, stability, and structure. Sputtering may be a preferable catalyst deposition method for integration with certain photoanodes, but optimizing conditions for codeposition of Ni and Fe at a desired composition in any individual sputtering system can be tedious, and some sputtering systems may be limited by the number of power sources or targets that can be used simultaneously, making codeposition unfeasible. Therefore, it may be more practical in certain circumstances to sequentially deposit Ni and Fe to form a layered structure. There may also be advantages to having either Ni(OOH) or Fe(OOH) as the layer in direct contact with the substrate, either to improve charge transfer between the catalyst and photoanode or adhesion of the catalyst to the substrate material. In fact, one recent study used NiOOH deposited on top of FeOOH as a way to engineer a more favorable interface

DOI: 10.1021/acs.jpcc.5b04776
J. Phys. Chem. C 2015, 119, 18303−18316

between a $BiVO_4$ semiconductor and the OER catalysts by reducing interface recombination.[7]

It would thus be useful to understand how such layered catalyst systems differ from codeposited catalysts, as this may have great implications on the design of optimized photoelectrode-catalyst interfaces. In this subsection, we compare the activity of catalysts prepared by sputtering where the elements were either deposited at the same time (codeposition) or with sequentially deposited layers of Ni and Fe. Previous work has shown that the presence of ppm or ppb levels of Fe impurities can greatly influence the OER activity of NiOOH catalysts,[23,38] indicating that Fe can migrate and incorporate into Ni with relative ease under appropriate conditions. We found that the order of the catalyst layers greatly affects the degree of mixing of the metal centers in sputtered catalyst films.

We sputter-deposited three types of films, each 2 nm thick with an overall as-deposited target composition of 50% Fe. One of these films was cosputtered 50:50 Fe/Ni (identical to the films discussed in the previous section, hereafter denoted as "mixed Ni−Fe"). The remaining two catalyst films were made by sputtering sequential layers of the Ni and Fe elements to form layered structures, one with Ni immediately adjacent to the underlying gold substrate and Fe on top of the Ni (Au/Ni/Fe, denoted from this point forward as "Fe-on-top"), and the second with Fe immediately adjacent to gold and Ni on top (Au/Fe/Ni, or "Ni-on-top").

Angle-resolved XPS profile analysis of each film type as-deposited and after electrochemical characterization is presented in Figure 9. The photoelectron inelastic mean free path (IMFP) is estimated to be ∼2 nm for both Ni and Fe using the 1254.6 eV Mg Kα excitation source, and the probability that inelastic scattering of emitted electrons will occur increases exponentially with increasing sample depth.[49] Therefore, the greatest contribution of signal in the photoelectron spectra originates from material closest to the sample surface; as higher takeoff angles are probed, further surface sensitivity is attained. The increased surface sensitivity is readily observed in the Au substrate contribution to the total signal from all metals, which for most samples decreases from 35 to 45% Au at a 0° takeoff angle to less than 20% Au at a 70° takeoff angle. (Note that in this section, percentages of individual metals are given as the percent of the total [Fe + Ni + Au], as determined by XPS).

In the as-deposited mixed Ni−Fe film, the amounts of Ni and Fe observed at each takeoff angle are similar, for example, 34% Fe and 31% Ni at 0°, and 41% Fe and 39% Ni at 70°, consistent with equal distribution of Ni and Fe throughout the film. For Ni-on-top, significantly more Ni is observed (∼50%) than Fe (∼16%) at 0°, and the relative amount of Ni further predominates (68%) at increased takeoff angles, while the % Fe is essentially constant at all takeoff angles. Similarly, the Fe-on-top sample exhibits greater Fe surface content (42%) compared to Ni (10%) at 0°; with a takeoff angle of 70°, an Fe content of 57% is observed, while the %Ni remains essentially constant. Since equal amounts of both Ni and Fe were deposited for each sample, the relative predominance of Ni for the Ni-on-top sample and Fe for the Fe-on-top confirms that a layered-type structure is formed as expected with sequential deposition of these films.

After electrochemical characterization, the Ni and Fe percentages are still highest for the Ni-on-top and Fe-on-top samples, respectively. The data for Fe-on-top show a lower Fe/Ni ratio across all takeoff angles than in the as-deposited film, which could be consistent with loss of some of the Fe capping layer. The mixed Ni−Fe sample has significantly more Ni content (60%) than Fe content (20%) at all takeoff angles, consistent with the loss of Fe during stabilization cycling discussed previously (a decrease of the as-deposited 50:50 Fe/Ni ratio to 25:75 Fe/Ni after electrochemical cycling and characterization).

It is important to comment on the similarities between the three plots in Figure 9 for as-deposited Ni-on-top and both Ni-on-top and mixed Ni−Fe after characterization. It is clear from knowledge of the deposition methods that a layered structure is present in the Ni-on-top sample as-deposited, which is consistent with the data in Figure 9. However, the data for Ni-on-top and mixed Ni−Fe after characterization are nearly identical to the data for as-deposited Ni-on-top. Therefore, in the case of the Ni-on-top film after electrochemical characterization, the angle-resolved XPS data alone cannot distinguish conclusively between a layered film and a mixed Ni−Fe film with unequal Ni and Fe contents. To determine whether significant mixing of the Ni and Fe layers is occurring during stabilization, cycling, and operation under electrochemical conditions, we compared data taken by cyclic voltammetry and in situ Raman spectroscopy.

The voltammograms of the sequentially and codeposited Ni−Fe films after electrochemical characterization are presented in Figure 10. The positions of the oxidation and reduction waves for Ni-on-top and mixed Ni−Fe nearly overlap. Furthermore, for all three samples, the positions of the Ni oxidation and reduction waves are shifted anodic relative to those of the 100% Ni samples (see Figure 1), indicating that the Ni and Fe are mixing in the layered-deposited films. A comparison of the OER region of the CVs shows a 1 mA cm^{-2} current density is observed at a similar potential for the Ni-on-top and mixed Ni−Fe films (∼0.65 V) but at a higher potential for Fe-on-top (∼0.67 V).

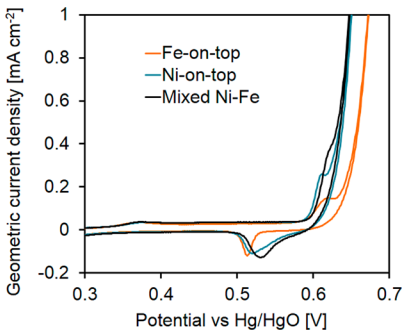

Figure 10. Cyclic voltammograms for sequentially (i.e., layered) and codeposited 50% Fe films over Au. CVs were collected in 0.1 M Fe-free KOH at a scan rate of 10 mV s^{-1} and RDE rotation rate of 1600 rpm.

Table 3 provides further details comparing the electrochemical behavior of the codeposited and layered samples. The geometric current density at η = 300 mV for Fe-on-top is significantly lower than those observed for Ni-on-top and mixed Ni−Fe films, while the Fe-on-top overpotential (at 10 mA cm^{-2} current density) is higher than that for the Ni-on-top and mixed Ni−Fe films by 59 and 45 mV, respectively. Additionally, we observe that the activity vs surface composition of the layered samples (18% Fe for Ni-on-top and 54% Fe for Fe-on-top, as determined by XPS at 0° takeoff

DOI: 10.1021/acs.jpcc.5b04776
J. Phys. Chem. C 2015, 119, 18303−18316

Table 3. Activity, Reduction Peak Area, and Surface Composition of Sequentially and Codeposited Ni−Fe Films after Electrochemical Cycling

	η = 0.3 V current density [mA cm^{-2}]	j = 10 mA cm^{-2} overpotential [mV]	reduction peak area [mC cm^{-2}]
Fe-on-top	0.3 ± 0.2	390 ± 4	97 ± 61
Ni-on-top	2.2 ± 0.3	331 ± 7	443 ± 234
mixed Ni−Fe	1.9 ± 0.4	344 ± 8	560 ± 168

after electrochemical characterization) agrees with the activity trends observed for the $Ni_{1-x}Fe_xOOH$ films discussed in the previous section (for direct comparison, see Figure S6.4).

In situ Raman spectra were acquired for both mixed and layered Ni−Fe films (after electrochemical stabilization) during a 1 mV s^{-1} scan from 0.0 to 0.7 V in 0.1 M Fe-free KOH (corresponding voltammograms are shown in Figure S6.3). In contrast to the Raman spectra of the electrodeposited and sputtered samples for Figures 5 and 6, which were acquired over roughened Au electrodes, polished Au electrodes were used to preserve the relative thickness and layering of the Ni-on-top, Fe-on-top, and mixed Ni−Fe films. Figure 11 shows the spectra collected over each film. The Ni-on-top and mixed Ni−Fe samples exhibit similar spectral features, with the 480/560 cm^{-1} features of NiOOH appearing at 0.4 V and higher potentials. In contrast, the Raman modes of NiOOH at 480/560 cm^{-1} are much less intense (even at 0.6 V) for the Fe-on-top sample, indicating less NiOOH formation after 15 h of electrochemical stabilization cycling. (Note that Raman is a bulk measurement, so a capping layer of Fe would not be expected to significantly screen signal from an underlying NiOOH or $Ni_{1-x}Fe_xOOH$ layer.)

From the analysis of the data above, it is clear that after electrochemical stabilization, the Ni-on-top film converts during electrochemical stabilization/characterization to a material similar to the stabilized mixed Ni−Fe film. The relative Fe/Ni ratios determined via angle-resolved XPS (Figure 9, 18% Fe for Ni-on top vs 24% Fe for mixed Ni−Fe) are comparable after electrochemical characterization, and the samples are also structurally and electrochemically comparable, with essentially indistinguishable OER activities and reduction peak positions (Table 3).

In contrast, distinct differences are observed for Fe-on-top films. As detailed in Table 3, the Ni reduction peak area is 97 mC cm^{-2} for Fe-on-top, significantly less than the 560 mC cm^{-2} reduction peak area for mixed Ni−Fe. Less NiOOH formation is also observed via in situ Raman (Figure 11) after oxidation of the Fe-on-top sample compared to the Ni-on-top and mixed Ni−Fe samples, indicating a lower conversion of the sputtered, metallic Ni to $Ni(OH)_2$/NiOOH for the Fe-on-top sample. This could be due to the Fe-capping layer acting as a nonporous barrier over some Ni sites, preventing access to the electrolyte and slowing the conversion process. The geometric current density at η = 0.3 V for Fe-on-top is 15% of that for mixed Ni−Fe, while the area of the CV reduction peak (indicative of the extent of NiOOH formation) for the Fe-on-top sample is 17% of that for the mixed Ni−Fe film. Previous investigations in our group support that it is Fe within a NiOOH structure which is critical for high oxygen evolution activity.[35] The close correlation between the reduction peak area ratio and observed oxygen evolution current are consistent with the finding that formation of the NiOOH parent structure is a critical requirement for high oxygen evolution activity over $Ni_{1-x}Fe_xOOH$ catalyst films.

In summary, Ni-on-top and mixed Ni−Fe sputtered films convert with electrochemical stabilization cycling to essentially indistinguishable materials with OER activity and structures comparable to electrodeposited $Ni_{1-x}Fe_xOOH$. In contrast, Fe-on-top layered films exhibit lower OER activity and a decreased formation of a NiOOH-type structure, indicating that the metallic Fe capping layer impedes electrochemical conversion of metallic Ni to NiOOH. This suggests that the formation of NiOOH precedes incorporation of Fe into highly active OER sites, and supports previous work showing that Fe sites within a NiOOH structure are the critical component for high OER activity.

4. CONCLUSIONS

We compared the activity and structure of electrodeposited vs sputter-deposited $Ni_{1-x}Fe_xOOH$ films for water-splitting

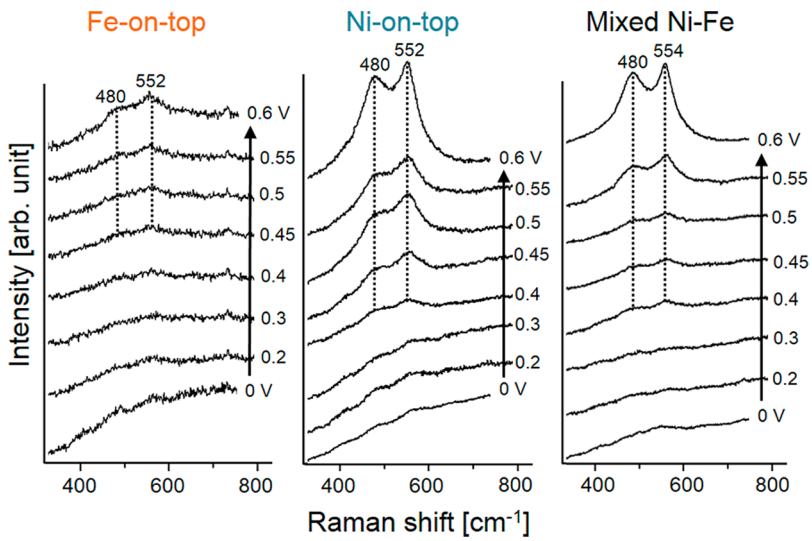

Figure 11. In situ Raman spectra for Fe-on-top, Ni-on-top, and mixed Ni−Fe films sputter-deposited on *polished* Au substrates as a function of potential vs Hg/HgO in 0.1 M Fe-free KOH, for which the OER equilibrium potential is 0.365 V.

DOI: 10.1021/acs.jpcc.5b04776
J. Phys. Chem. C 2015, 119, 18303−18316

applications in alkaline electrolyte. Films produced by sputter deposition are initially metallic but convert to metal (oxy)-hydroxide after 15 h of electrochemical stabilization cycling. During this conversion, a significant amount of Fe leaches from the sputtered films. In contrast, electrodeposited films are predominantly deposited as hydroxides and maintain the as-deposited Fe/Ni ratio. $Ni_{1-x}Fe_xOOH$ films exhibit significantly higher OER activities compared to pure Ni or Fe (oxy)-hydroxide, with $Ni_{1-x}Fe_xOOH$ films containing ∼20% Fe exhibiting the highest OER activity (j = ∼3 mA cm^{-2} at 300 mV overpotential, and ∼320 mV overpotential at j = 10 mA cm^{-2}). In situ Raman spectroscopy reveals that 25% Fe films deposited by both methods have similar structures after electrochemical stabilization, and the spectra are suggestive of a predominantly nickel−iron (oxy)hydroxide-type structure. Optimal OER activity coincides with the maximum Fe content which maintains a single Ni−Fe oxy(hydroxide)-type phase; above ∼20% Fe, a separate Fe-rich phase is formed, which appears significantly less OER-active.

Sputter deposition was also used to compare codeposited and layered films. Ni-on-top layered films are found to transform during electrochemical cycling to produce a film with indistinguishable structure and activity to that of codeposited 50:50 Fe/Ni. In contrast, Fe-on-top films exhibit a greater Fe surface concentration, which appears to impede the transformation of sputter-deposited Ni metal to Ni (oxy)-hydroxide, resulting in a significantly reduced OER activity. These findings demonstrate that $Ni_{1-x}Fe_xOOH$ catalyst films deposited by either sputter deposition or electrodeposition are similar in structure and OER activity, enabling the use of either technique for catalyst deposition over photoanode substrates.

■ ASSOCIATED CONTENT

Supporting Information

Additional experimental procedures, supplementary electrochemical data, X-ray photoelectron spectra. The Supporting Information is available free of charge on the ACS Publications website at DOI: 10.1021/acs.jpcc.5b04776.

■ AUTHOR INFORMATION

Corresponding Author

*E-mail: bell@cchem.berkeley.edu.

Author Contributions

†S.K. and M.W.L. contributed equally.

Notes

The authors declare no competing financial interest.

■ ACKNOWLEDGMENTS

This material is based upon work performed by the Joint Center for Artificial Photosynthesis, a DOE Energy Innovation Hub, supported through the Office of Science of the U.S. Department of Energy under Award Number DE-SC0004993. M.W.L. was partially supported by the University of California President's Postdoctoral Fellowship Program. The authors gratefully acknowledge Le Chen and Alan Lyon (Joint Center for Artificial Photosynthesis) for helpful discussions and assistance with sputter deposition, Jason Cooper and Jinhui Yang for assistance with XPS measurements, and Eric Granlund (University of California, Berkeley, College of Chemistry) for the fabrication of our electrode and sputtering components.

■ REFERENCES

(1) Matsumoto, Y.; Sato, E. Electrocatalytic Properties of Transition-Metal Oxides for Oxygen Evolution Reaction. *Mater. Chem. Phys.* **1986**, *14*, 397−426.

(2) Trotochaud, L.; Ranney, J. K.; Williams, K. N.; Boettcher, S. W. Solution-Cast Metal Oxide Thin Film Electrocatalysts for Oxygen Evolution. *J. Am. Chem. Soc.* **2012**, *134*, 17253−17261.

(3) Corrigan, D. A.; Bendert, R. M. Effect of Coprecipitated Metal-Ions on the Electrochemistry of Nickel-Hydroxide Thin-Films - Cyclic Voltammetry in 1M KOH. *J. Electrochem. Soc.* **1989**, *136*, 723−728.

(4) Smith, R. D. L.; Prevot, M. S.; Fagan, R. D.; Zhang, Z. P.; Sedach, P. A.; Siu, M. K. J.; Trudel, S.; Berlinguette, C. P. Photochemical Route for Accessing Amorphous Metal Oxide Materials for Water Oxidation Catalysis. *Science* **2013**, *340*, 60−63.

(5) McCrory, C. C. L.; Jung, S. H.; Peters, J. C.; Jaramillo, T. F. Benchmarking Heterogeneous Electrocatalysts for the Oxygen Evolution Reaction. *J. Am. Chem. Soc.* **2013**, *135*, 16977−16987.

(6) Lin, F. D.; Boettcher, S. W. Adaptive Semiconductor/Electrocatalyst Junctions in Water-Splitting Photoanodes. *Nat. Mater.* **2014**, *13*, 81−86.

(7) Kim, T. W.; Choi, K. S. Nanoporous $BiVO_4$ Photoanodes with Dual-Layer Oxygen Evolution Catalysts for Solar Water Splitting. *Science* **2014**, *343*, 990−994.

(8) Park, Y.; McDonald, K. J.; Choi, K. S. Progress in Bismuth Vanadate Photoanodes for Use in Solar Water Oxidation. *Chem. Soc. Rev.* **2013**, *42*, 2321−2337.

(9) Seabold, J. A.; Choi, K. S. Efficient and Stable Photo-Oxidation of Water by a Bismuth Vanadate Photoanode Coupled with an Iron Oxyhydroxide Oxygen Evolution Catalyst. *J. Am. Chem. Soc.* **2012**, *134*, 2186−2192.

(10) Kenney, M. J.; Gong, M.; Li, Y. G.; Wu, J. Z.; Feng, J.; Lanza, M.; Dai, H. J. High-Performance Silicon Photoanodes Passivated with Ultrathin Nickel Films for Water Oxidation. *Science* **2013**, *342*, 836−840.

(11) Yang, J. H.; et al. Efficient and Sustained Photoelectrochemical Water Oxidation by Cobalt Oxide/Silicon Photoanodes with Nanotextured Interfaces. *J. Am. Chem. Soc.* **2014**, *136*, 6191−6194.

(12) Trotochaud, L.; Mills, T. J.; Boettcher, S. W. An Optocatalytic Model for Semiconductor-Catalyst Water-Splitting Photoelectrodes Based on in Situ Optical Measurements on Operational Catalysts. *J. Phys. Chem. Lett.* **2013**, *4*, 931−935.

(13) Hu, C. C.; Wu, Y. R. Bipolar Performance of the Electroplated Iron-Nickel Deposits for Water Electrolysis. *Mater. Chem. Phys.* **2003**, *82*, 588−596.

(14) Potvin, E.; Brossard, L. Electrocatalytic Activity of Ni-Fe Anodes for Alkaline Water Electrolysis. *Mater. Chem. Phys.* **1992**, *31*, 311−318.

(15) Corrigan, D. A. The Catalysis of the Oxygen Evolution Reaction by Iron Impurities in Thin-Film Nickel-Oxide Electrodes. *J. Electrochem. Soc.* **1987**, *134*, 377−384.

(16) Li, X. H.; Walsh, F. C.; Pletcher, D. Nickel Based Electrocatalysts for Oxygen Evolution in High Current Density, Alkaline Water Electrolysers. *Phys. Chem. Chem. Phys.* **2011**, *13*, 1162−1167.

(17) Singh, R. N.; Pandey, J. P.; Anitha, K. L. Preparation of Electrodeposited Thin Films of Nickel-Iron Alloys on mild Steel for Alkaline Water Electrolysis. Part I: Studies on Oxygen Evolution. *Int. J. Hydrogen Energy* **1993**, *18*, 467−473.

(18) Seabold, J. A.; Choi, K.-S. Effect of a Cobalt-Based Oxygen Evolution Catalyst on the Stability and the Selectivity of Photo-Oxidation Reactions of a WO_3 Photoanode. *Chem. Mater.* **2011**, *23*, 1105−1112.

(19) Hamann, T. W. Splitting Water with Rust: Hematite Photoelectrochemistry. *Dalton Trans* **2012**, *41*, 7830−7834.

(20) Walter, M. G.; Warren, E. L.; McKone, J. R.; Boettcher, S. W.; Mi, Q. X.; Santori, E. A.; Lewis, N. S. Solar Water Splitting Cells. *Chem. Rev.* **2010**, *110*, 6446−6473.

(21) Gamelin, D. R. Water Splitting Catalyst or Spectator? *Nat. Chem.* **2012**, *4*, 965−967.

DOI: 10.1021/acs.jpcc.5b04776
J. Phys. Chem. C 2015, 119, 18303−18316

(22) Miller, E. L.; Rocheleau, R. E. Electrochemical Behavior of Reactively Sputtered Iron-Doped Nickel Oxide. *J. Electrochem. Soc.* **1997**, *144*, 3072−3077.
(23) Trotochaud, L.; Young, S. L.; Ranney, J. K.; Boettcher, S. W. Nickel-Iron Oxyhydroxide Oxygen-Evolution Electrocatalysts: The Role of Intentional and Incidental Iron Incorporation. *J. Am. Chem. Soc.* **2014**, *136*, 6744−6753.
(24) Louie, M. W.; Bell, A. T. An Investigation of Thin-Film Ni-Fe Oxide Catalysts for the Electrochemical Evolution of Oxygen. *J. Am. Chem. Soc.* **2013**, *135*, 12329−12337.
(25) *NIST X-Ray Photoelectron Spectroscopy Database*, version 4.1; National Institute of Standards and Technology: Gaithersburg, MD, 2012; http://srdata.nist.gov/xps/.
(26) Kostecki, R.; McLarnon, F. Electrochemical and in Situ Raman Spectroscopic Characterization of Nickel Hydroxide Electrodes. *J. Electrochem. Soc.* **1997**, *144*, 485−493.
(27) Lyons, M. E. G.; Brandon, M. P. The Oxygen Evolution Reaction on Passive Oxide Covered Transition Metal Electrodes in Aqueous Alkaline Solution. Part 1-Nickel. *Int. J. Electrochem Sci.* **2008**, *3*, 1386−1424.
(28) Landon, J.; Demeter, E.; Inoglu, N.; Keturakis, C.; Wachs, I. E.; Vasic, R.; Frenkel, A. I.; Kitchin, J. R. Spectroscopic Characterization of Mixed Fe-Ni Oxide Electrocatalysts for the Oxygen Evolution Reaction in Alkaline Electrolytes. *ACS Catal.* **2012**, *2*, 1793−1801.
(29) Klaus, S.; Cai, Y.; Louie, M. W.; Trotochaud, L.; Bell, A. T. Effects of Fe Electrolyte Impurities on $Ni(OH)_2$/NiOOH Structure and Oxygen Evolution Activity. *J. Phys. Chem. C* **2015**, *119*, 7243−7254.
(30) Wehrens-Dijksma, M.; Notten, P. H. L. Electrochemical Quartz Microbalance Characterization of $Ni(OH)_2$-Based Thin Film Electrodes. *Electrochim. Acta* **2006**, *51*, 3609−3621.
(31) Lee, J.-W.; Han, J.-N.; Seo, M.; Pyun, S.-I. Transport of Alkaline Cation and Neutral Species through the α-$Ni(OH)_2$/γ-NiOOH Film Electrode. *J. Solid State Electrochem.* **2001**, *5*, 459−465.
(32) Singh, R. N.; Pandey, J. P.; Anitha, K. L. Preparation of Electrodeposited Thin Films of Nickel-Iron Alloys on Mild Steel for Alkaline Water Electrolysis. Part I: Studies on Oxygen Evolution. *Int. J. Hydrogen Energy* **1993**, *18*, 467−473.
(33) Miller, E. L.; Rocheleau, R. E. Electrochemical Behavior of Reactively Sputtered Iron-Doped Nickel Oxide. *J. Electrochem. Soc.* **1997**, *144*, 3072−3077.
(34) Landon, J.; Demeter, E.; İnoğlu, N.; Keturakis, C.; Wachs, I. E.; Vasić, R.; Frenkel, A. I.; Kitchin, J. R. Spectroscopic Characterization of Mixed Fe−Ni Oxide Electrocatalysts for the Oxygen Evolution Reaction in Alkaline Electrolytes. *ACS Catal.* **2012**, *2*, 1793−1801.
(35) Friebel, D.; et al. Identification of Highly Active Fe Sites in (Ni,Fe)OOH for Electrocatalytic Water Splitting. *J. Am. Chem. Soc.* **2015**, *137*, 1305−1313.
(36) Burke, M. S.; Kast, M. G.; Trotochaud, L.; Smith, A. M.; Boettcher, S. W. Cobalt−Iron (Oxy)Hydroxide Oxygen Evolution Electrocatalysts: The Role of Structure and Composition on Activity, Stability, and Mechanism. *J. Am. Chem. Soc.* **2015**, *137*, 3638−3648.
(37) Desilvestro, J.; Corrigan, D. A.; Weaver, M. J. Characterization of Redox States of Nickel-Hydroxide Film Electrodes by in Situ Surface Raman-Spectroscopy. *J. Electrochem. Soc.* **1988**, *135*, 885−892.
(38) Johnston, C.; Graves, P. R. in Situ Raman-Spectroscopy Study of the Nickel Oxyhydroxide Electrode (NOE) System. *Appl. Spectrosc.* **1990**, *44*, 105−115.
(39) Bernard, M. C.; Bernard, P.; Keddam, M.; Senyarich, S.; Takenouti, H. Characterisation of New Nickel Hydroxides During the Transformation of α-$Ni(OH)_2$ to β-$Ni(OH)_2$ by Ageing. *Electrochim. Acta* **1996**, *41*, 91−93.
(40) Hall, D. S.; Lockwood, D. J.; Poirier, S.; Bock, C.; MacDougall, B. R. Applications of in Situ Raman Spectroscopy for Identifying Nickel Hydroxide Materials and Surface Layers During Chemical Aging. *ACS Appl. Mater. Interfaces* **2014**, *6*, 3141−3149.
(41) Hibben, J. H. The Raman Spectra of Water, Aqueous Solutions and Ice. *J. Chem. Phys.* **1937**, *5*, 166−172.
(42) Yeo, B. S.; Klaus, S. L.; Ross, P. N.; Mathies, R. A.; Bell, A. T. Identification of Hydroperoxy Species as Reaction Intermediates in the Electrochemical Evolution of Oxygen on Gold. *ChemPhysChem* **2010**, *11*, 1854−1857.
(43) Cordoba de Torresi, S. I.; Provazi, K.; Malta, M.; Torresi, R. M. Effect of Additives in the Stabilization of the α Phase of $Ni(OH)_2$ Electrodes. *J. Electrochem. Soc.* **2001**, *148*, A1179−A1184.
(44) Cornilsen, B. C.; Karjala, P. J.; Loyselle, P. L. Structural Models for Nickel Electrode Active Mass. *J. Power Sources* **1988**, *22*, 351−357.
(45) Lu, Z.; Xu, W.; Zhu, W.; Yang, Q.; Lei, X.; Liu, J.; Li, Y.; Sun, X.; Duan, X. Three-Dimensional NiFe Layered Double Hydroxide Film for High-Efficiency Oxygen Evolution Reaction. *Chem. Commun.* **2014**, *50*, 6479−6482.
(46) Biesinger, M. C.; Payne, B. P.; Lau, L. W. M.; Gerson, A.; Smart, R. S. C. X-ray Photoelectron Spectroscopic Chemical State Quantification of Mixed Nickel Metal, Oxide and Hydroxide Systems. *Surf. Interface Anal.* **2009**, *41*, 324−332.
(47) Temesghen, W.; Sherwood, P. M. A. Analytical Utility of Valence Band X-ray Photoelectron Spectroscopy of Iron and its Oxides, with Spectral Interpretation by Cluster and Band Structure Calculations. *Anal. Bioanal. Chem.* **2002**, *373*, 601−608.
(48) McIntyre, N. S.; Zetaruk, D. G. X-ray Photoelectron Spectroscopic Studies of Iron Oxides. *Anal. Chem.* **1977**, *49*, 1521−1529.
(49) Powell, C. J. The Quest for Universal Curves to Describe the Surface Sensitivity of Electron Spectroscopies. *J. Electron Spectrosc. Relat. Phenom.* **1988**, *47*, 197−214.

DOI: 10.1021/acs.jpcc.5b04776
J. Phys. Chem. C 2015, 119, 18303−18316